Appl. Phys. A (2015) 118:885–892
DOI 10.1007/s00339-014-8805-5

Applied Physics A
Materials Science & Processing

Combined effects of defects and hydroxyl groups on the electronic transport properties of reduced graphene oxide

Xiao Liu · Yanwei Wen · Bin Shan · Kyeongjae Cho · Z. Chen · Rong Chen

Received: 12 August 2014 / Accepted: 23 September 2014 / Published online: 2 October 2014

Abstract The effects of four typical defects on the hydroxyl groups' migration and the conductivity of graphene have been studied using density functional theory and nonequilibrium Green's function formalism. An obvious anisotropy of the diffusion barriers along different paths is correlated to the symmetric behavior of spin-polarized charge density around the defects. The migration energy scenario indicates that the defects effectively hinder the hydroxyl groups' migration toward them, indicating that most hydroxyl groups could be stabilized outside the defect region in reduced graphene oxide. Through the electronic transport calculations and local density of states analysis, hydroxyl groups locating outside of the defect region will cause the transport channels near the Fermi level to disappear and reduce the conductance considerably.

X. Liu · R. Chen (✉)
State Key Laboratory of Digital Manufacturing Equipment and Technology and School of Mechanical Science and Engineering, Huazhong University of Science and Technology, Wuhan 430074, Hubei, People's Republic of China
e-mail: rongchen@mail.hust.edu.cn

Y. Wen · B. Shan · Z. Chen (✉)
State Key Laboratory of Material Processing and Die and Mould Technology and School of Materials Science and Engineering, Huazhong University of Science and Technology, Wuhan 430074, Hubei, People's Republic of China
e-mail: AlexChenL2014@gmail.com

B. Shan · K. Cho
Department of Materials Science and Engineering, The University of Texas at Dallas, Richardson, TX 75080, USA

1 Introduction

Graphene has aroused great interest for its excellent mechanical, electronic, and chemical properties since its discovery [1, 2]. To promote its potential applications in large-scale nanoelectronic devices, many approaches have been developed to mass-produce high-quality graphene. The route via reduction of graphene oxide (GO) is regarded as one of the most promising approaches for the large-scale production of graphene, comparing with micromechanical exfoliation, epitaxial growth, and chemical vapor deposition [3]. Thermal reduction [4, 5] and chemical reduction [6, 7] are two typical processes applied in the reduction process of GO, which generally has considerable amount of hydroxyl and epoxy groups on graphene plane [8–11]. After the reduction process, the achievable C/O ratio ranges from 2 ∼ 4:1 to about 12 ∼ 15:1 [12, 13] and the reduced graphene oxide (RGO) shows significant improvement in conductance by 3 or 4 orders [14–16]. Similar to GO, the functional groups on RGO are also found mainly to be hydroxyl and epoxy by the X-ray photoelectron spectrums [17, 18]. These studies suggest that the electronic transport properties of RGO are closely related to the functional groups and defects [3]. Very recent works show that epoxy groups on GO are metastable under ambient conditions and will transform to hydroxyl groups gradually in a few months [19, 20], which suggests that the hydroxyls are the most abundant and stable functional groups on GO and RGO. Besides functional groups, topological defects are also common on RGO [21]. However, the distribution of hydroxyl groups on RGO and the synergetic effect of hydroxyl and structural defects on transport properties still remain elusive. For example, it was hypothesized that hydroxyl groups are mobile on GO and they reside in

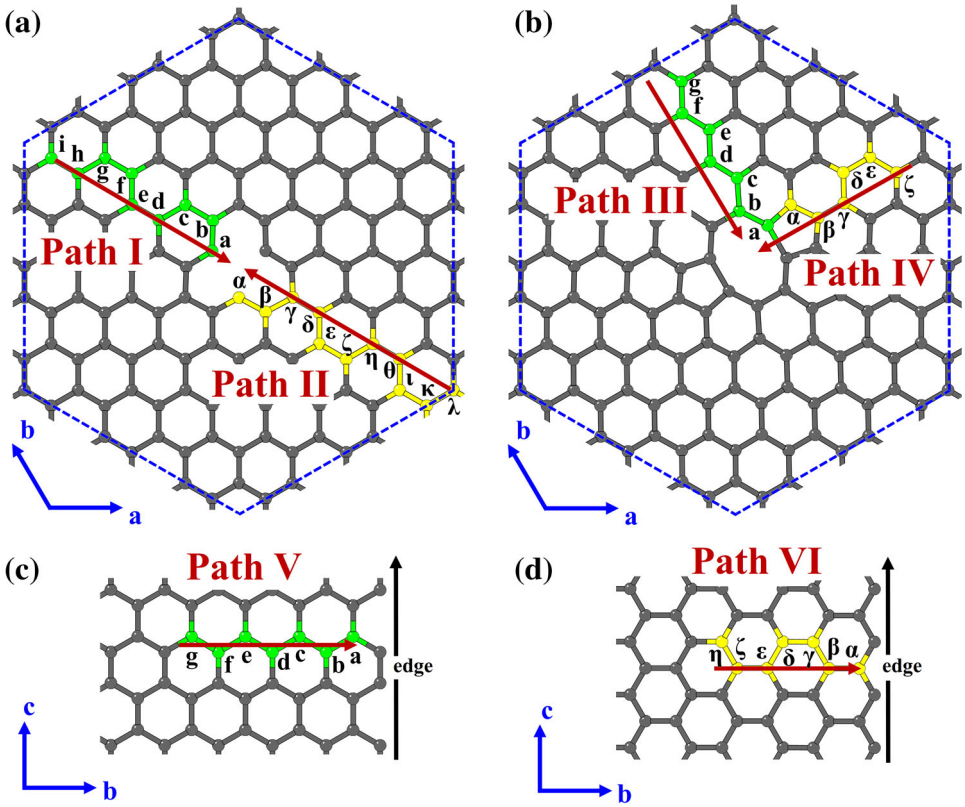

Fig. 1 Diffusion paths of hydroxyl on graphene with **a** single vacancy (path I and path II), **b** di-vacancy (path III and path IV), **c** and **d** armchair and zigzag edges (path V and path VI). The diffusion carbon sites have been highlighted with *yellow* (zigzag direction) and *green* direction (armchair direction). **c** and **d** are just partly shown in 8-AGNR and 8-ZGNR

defects region mostly [3]. However, recent molecular dynamics (MD) simulations indicate that hydroxyl appear both in and out of the defects region [20, 22, 23]. The different configurations of hydroxyl and defects on graphene may lead to significant changes of the electronic transport properties.

In this letter, the role of defects and hydroxyl groups is investigated to clarify how they affect the structural and transport properties of RGO. Anisotropic diffusion barriers have been found along different paths: One increases monotonously and the other is oscillatory. Moreover, the migration of hydroxyl on all paths is more difficult than that on pristine graphene, which indicates that most hydroxyl groups could be stabilized outside the defect region in RGO. The spin-polarized charge density analysis shows that the magnitude of diffusion barriers can be correlated to the charge density around the defects. We further show that for high oxygen concentration, the presence of hydroxyl groups out of the defect has larger effect on the RGO conductance, compared with hydroxyl groups inside the defects. The π-electron local density of states (LDOS) is performed to elucidate the difference between hydroxyl inside and outside the defects. The results imply that the hydroxyl out of the defects will lead to the disappearance of the transport channels, which degrades the electronic conductance seriously.

2 Computational methods

The spin-polarized density functional theory (DFT) [24, 25] calculations are carried out using plane waves as implemented in Vienna ab initio simulation package (VASP) [26–28]. The exchange and correlation energy are treated by generalized gradient approximation (GGA) with Perdew–Burke–Ernzerhof (PBE) [29] form generated by the projector augmented wave (PAW) [30] method. The geometry optimization is considered complete when the Hellmann–Feynman force on each atom is <0.05 eV/Å and an energy cutoff of 400 eV is employed on the plane wave basis. The *k* points are sampled on a Monkhorst–Pack [31] grid of 15 × 15 × 1 for a 1 × 1 graphene unit cell. In order to avoid image interactions, we have adopted a 8 × 8 hexagonal graphene supercell of 19.68 Å × 19.68 Å and a vacuum thickness of 14 Å. We have also employed rectangular graphene nanoribbon (GNR) supercells. The vectors of GNR in *c* direction (symmetric direction) are larger than 12 Å to avoid the lateral interaction between hydroxyl groups in two adjacent unit cells. A climbing image-nudged elastic band (CI-NEB) [32] calculation is used to calculate the minimum energy path (MEP) and to find the saddle points between two local minima for the system. Eight intermediate images are used for all CI-NEB calculations, which can map the MEP with reasonable accuracy.

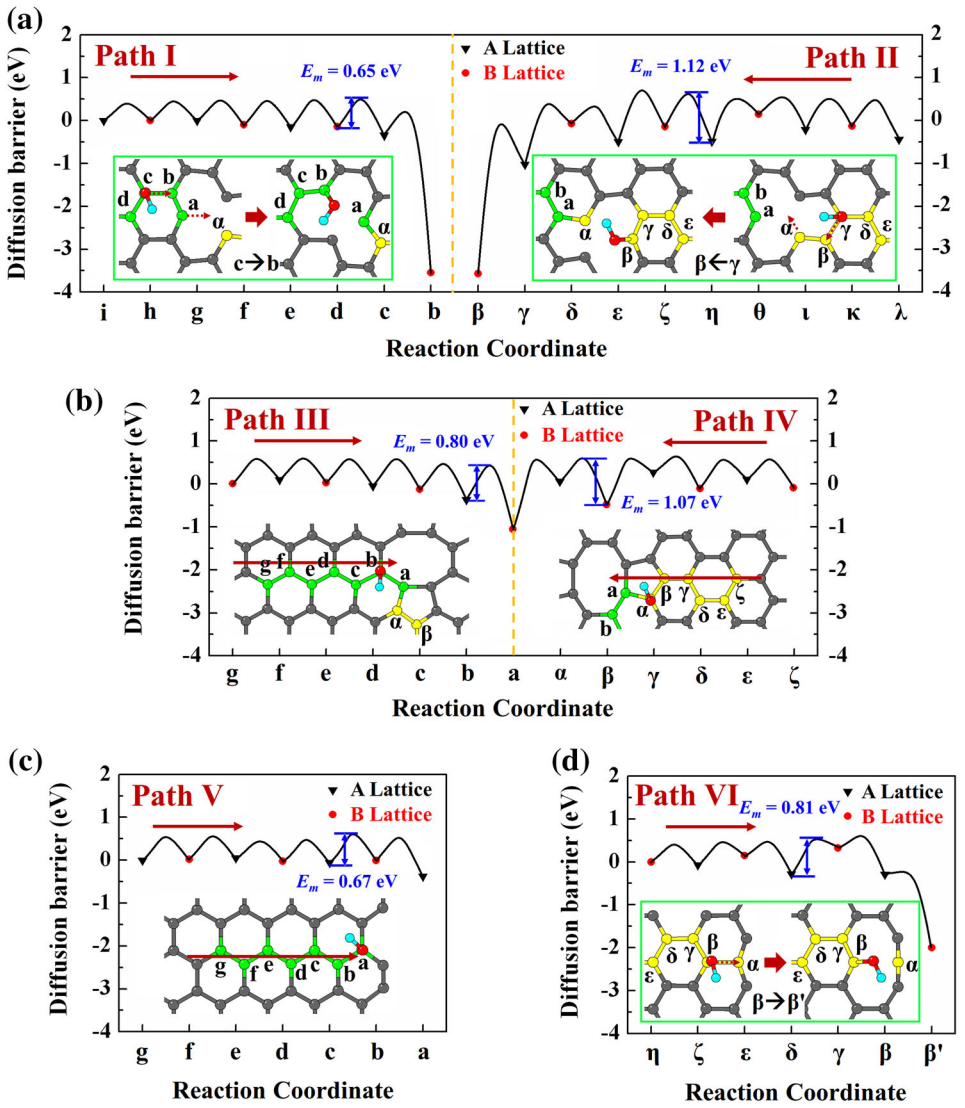

Fig. 2 Diffusion barriers of hydroxyl migration along path I–VI. The total energies of the structure with hydroxyl adsorbed on the first carbon site are set to zero. The highest energy barriers in each migration path are labeled as E_m. A and B lattices are labeled by triangle and circle, respectively

The transport properties are analyzed using the TranSIESTA program implemented in the SIESTA package [33, 34] based on nonequilibrium Green's function (NEGF) [35] formalism with the device structures optimized by VASP. The GGA and single-ζ plus polarization (SZP) basis set are selected, and cutoff is set to 2,040 eV, which have been confirmed the validity of these setting in such systems [36]. A total of 101 *k* points are used in transport calculations to reproduce the semi-infinite and the transmission spectrums are calculated with 251 *k* points in *c* direction, the convergence of which has been tested.

3 Results and discussion

Single vacancies (SVs) and double vacancies (DVs) are the most common defects on graphene [37, 38]. Previous study has also evidenced the existence of larger structural defects on RGO fragments [21]. Thus, besides SVs and DVs in graphene, we have also used GNRs with armchair (AGNR) and zigzag (ZGNR) edges to simulate the hydroxyl groups' migration toward the edge of RGO sheets. Figure 1a, b shows the periodic graphene model of 8 × 8 supercell with SV and DV. SV has been observed to be reconstructed into pentagonal carbon rings [39]. Our calculations also indicate that the SV is reconstructed spontaneously with local stress around the vacancy, while the DV center is relaxed to form a stable octagonal ring. According to the symmetry, graphene with SVs and DVs belong to C_{3v} and C_{2v} groups, respectively. Thus, the angle between two high-symmetry diffusion paths on SV graphene is 180°, and the two paths on DV graphene are orthogonal, as marked as green and yellow in Fig. 1a, b for SV and DV graphene, respectively. Figure 1c, d highlights the diffusion paths of hydroxyl from the center to the edge of 8-AGNR and 8-ZGNR.

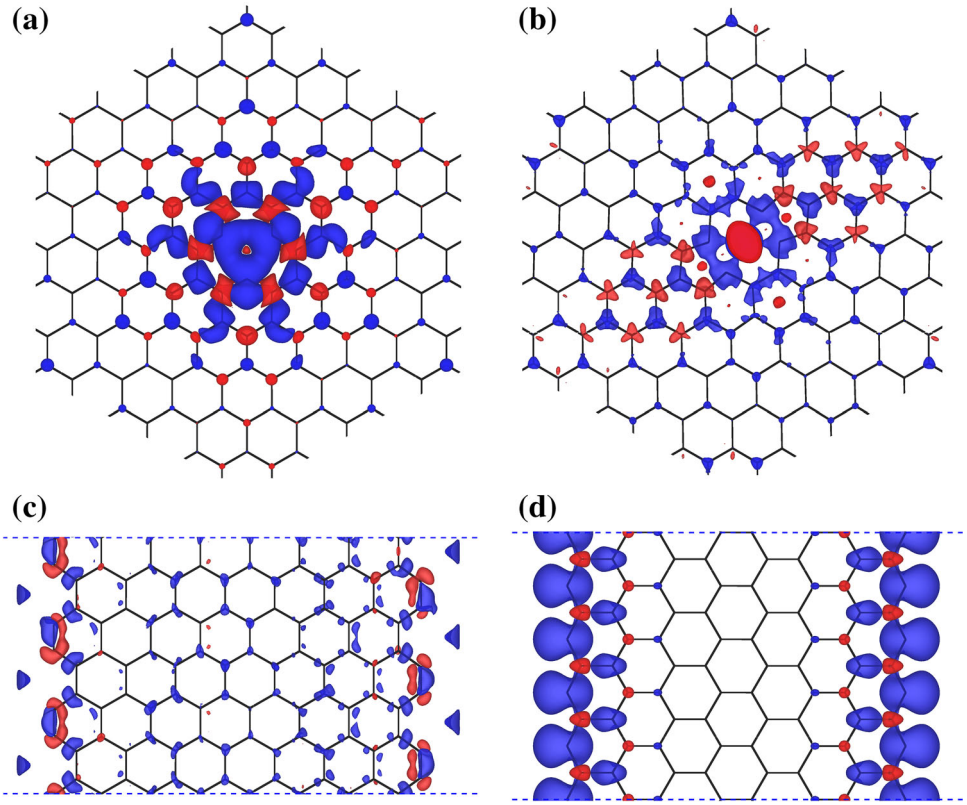

Fig. 3 Spin-polarized charge density (spin up minus spin down) of graphene with **a** SV, **b** DV, **c** and **d** armchair and zigzag edges. The *blue area* represents spin up and *red area* represents spin down. The isosurface levels are 1E-5a_0^{-3} in **a**, 4E-7a_0^{-3} in **b**, 3E-7a_0^{-3} in **c** and 4E-3a_0^{-3} in **d**, respectively, where a_0 is the Bohr radius

The MEP of hydroxyl group diffusing along each path on graphene plane in the SV case is shown in Fig. 2a. According to the two inequivalent sub-lattices in graphene superlattice, the carbon adsorption sites have been divided into A and B sub-lattices, which are labeled by triangle and circle, respectively. In previous study, the diffusion barrier of a hydroxyl group on graphene was calculated to be about 0.35 eV [19, 40], and people generally assume that hydroxyl was highly mobile on graphene. When the hydroxyl group is far away ($\sim$10 Å) from the SV, the diffusion barrier E_{diff} (0.37 eV) from *i* to h is close to that of pristine graphene. However, E_{diff}s increase sharply when the hydroxyl gets closer to the SV. When the hydroxyl travels from *i* to *b* along path I, the highest diffusion barrier E_{m} increases to 0.65 eV and E_{m} along path II even reaches to 1.12 eV, almost three times larger than that of pristine graphene. These results reveal that the hydroxyl becomes less mobile as it approaches to the SV. Moreover, it is interesting that the E_{diff} along the two paths shows distinctive behaviors. Along path I, the barriers from A(B) to B(A) lattice increase monotonically when the hydroxyl moves toward the SV. In contrast, barriers oscillate considerably when the hydroxyl travels along path II, which is similar to the previous reported "odd–even oscillation" in ZGNR [41, 42]. Such difference can be attributed to the different binding energies between the hydroxyl and C atoms along the two paths. Along path I, the binding energy (E_{b}) of the hydroxyl at each site is close to each other and decreases slowly as it approaches the SV. Along path II, E_{b}s of hydroxyl oscillate with the hydroxyl migration barriers on A and B sub-lattices. On the other hand, the structural reconstruction will occur during the last migration step as the atomic structures shown in Fig. 2a. During the migration procedure of $c \rightarrow b$, the a site C atom will fill the SV so that hydroxyl will reach into the defects and form a stable configuration. The same behavior will also happen during the migration procedure of $\gamma \rightarrow \beta$.

Figure 2b presents the MEP of hydroxyl moving to DV center along path III and path IV. E_{diff}s along the two paths exhibit the same behavior as those of SV, and the E_{m}s are 0.80 eV ($b \rightarrow a$) and 1.07 eV ($\beta \rightarrow \alpha$), respectively. Since DV center has formed a stable octagonal ring, no structural reconstruction is observed when the hydroxyl migrates to DV region. The MEPs of the hydroxyl migrating from the center to the edge of AGNR and ZGNR are shown in Fig. 2c, d. The same reconstruction as SV will occur when hydroxyl is close to the zigzag edge which may indicate that the zigzag edge is more unstable than the armchair edge. It is interesting that the E_{diff} along path V and path VI follows the same trend as path I(II) and path II(IV), with the E_{m}s of 0.67 eV ($c \rightarrow d$) and 0.81 eV ($\delta \rightarrow \gamma$), respectively. Thus, these migration paths can be classified

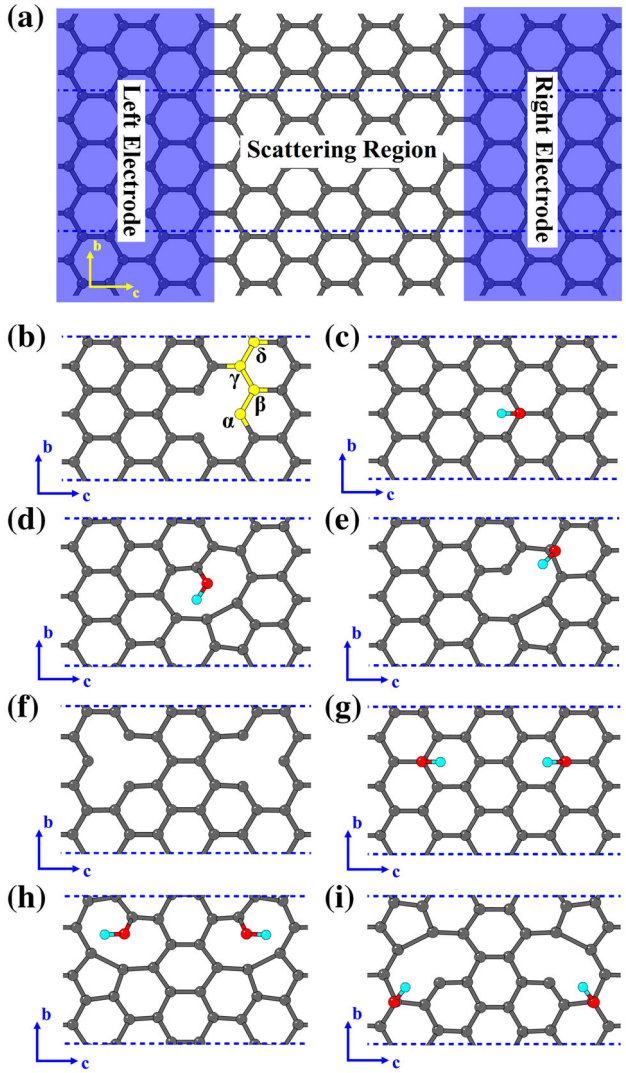

Fig. 4 **a** Atomic model for transport calculations. Left and right electrodes consist of semi-infinite pristine graphene sheets. The scattering region in **a** is pristine graphene consisted of periodic unit of three armchair chains. **b**–**i** are the scattering regions of RGO with difference vacancy and hydroxyl situations **b** SV, **c** hydroxyl, **d** hydroxyl in SV, **e** hydroxyl out of SV, **f** two SVs, **g** two hydroxyl groups, **h** two hydroxyl groups in SVs, and **i** two hydroxyl groups out of SVs

into two groups (path I, III, V and path II, IV, VI) according to the E_{diff}-changing behavior. No matter which group paths, the increased E_{diff}s for the four cases in Fig. 2 suggest that the implantation of defect hinders the migration of the hydroxyl. Moreover, a correlation can be found between the energy barrier and the binding energy of the hydroxyl.

To shed light on the origin of the barrier difference along two migration paths, the spin-polarized charge density $\rho(\mathbf{r})$ of graphene with different defects is represented in Fig. 3. $\rho(\mathbf{r})$ of SV graphene (Fig. 3a) presents C_{3v}-symmetry. It is found that the $\rho(\mathbf{r})$ of C atoms along path I increases monotonically, while that along path II fluctuates alternatively between A and B lattices. Figure 3b shows the calculated spin-polarized charge density of DV graphene. We can also easily find that there are also two type paths according to the changing behavior of $\rho(\mathbf{r})$ of C atoms which is similar to that of SV graphene. We have also calculated the $\rho(\mathbf{r})$ of AGNR and ZGNR as shown in Fig. 3c, d, respectively, which are similar as previous calculations [43]. The $\rho(\mathbf{r})$ away from the edge in AGNR is positive and uniform. However, the $\rho(\mathbf{r})$ will be larger for the C atoms near the edge. The odd–even oscillation has also been found in our calculation. For all cases in Fig. 3, it is clear that the spin-polarized charge density distribution correlates well with the binding energy behavior of the hydroxyl on the graphene with defect along the paths. As the hydroxyl group is covalently bonded to the carbon atoms near the defect region in graphene, the isolated charge density on each site would mostly determine the bonding strength of hydroxyl–carbon, as well as the migration energy barrier.

Besides the defect edges dependence, higher energy barriers suggest that the diffusion of the hydroxyl near the defect is hindered. As a result, the hydroxyl has considerable probability for staying outside of defects, which has also been confirmed by MD simulations [20, 22, 23]. Together with the fact of high C/O ratio in RGO, many hydroxyl groups are expected to be distributed away from the defects. In previous study, Lee et al. [44] showed that electronic transport properties of RGO will be slightly improved when hydroxyl groups locate inside the defect. Huang et al. [46] and Dai et al. [45] showed that the bandgap of RGO is related to the oxygen coverage. They only focus on the effect of oxygen concentration, and the defects have not been considered in their study. Here, we present comprehensive NEGF calculations of the electronic transport properties of RGO with hydroxyl group both inside and outside the defect, as well as the effect of the concentration of hydroxyl groups. The structural model of the device for transport calculations is shown in Fig. 4a, in which the c axis is the transport direction and the unit cell is periodic along the b axis. We have considered hydroxyl inside and outside of SV with C/O about 36:1 and 18:1, representing two different oxygen concentrations. The initial position of hydroxyl outside of SV is located at γ-site, which has the strongest adsorption energy among the sites out of defects and a forward diffusion barrier of 0.94 eV, as shown in Fig. 2a. The transmission spectrum of the graphene with only SV or hydroxyl is considered for comparison, and the scattering structures are shown in Fig. 4b–i. To verify the stability of these structures, MD simulations using the LAMMPS package [47] with ReaxFF reactive force field [48] at 600 K are performed.

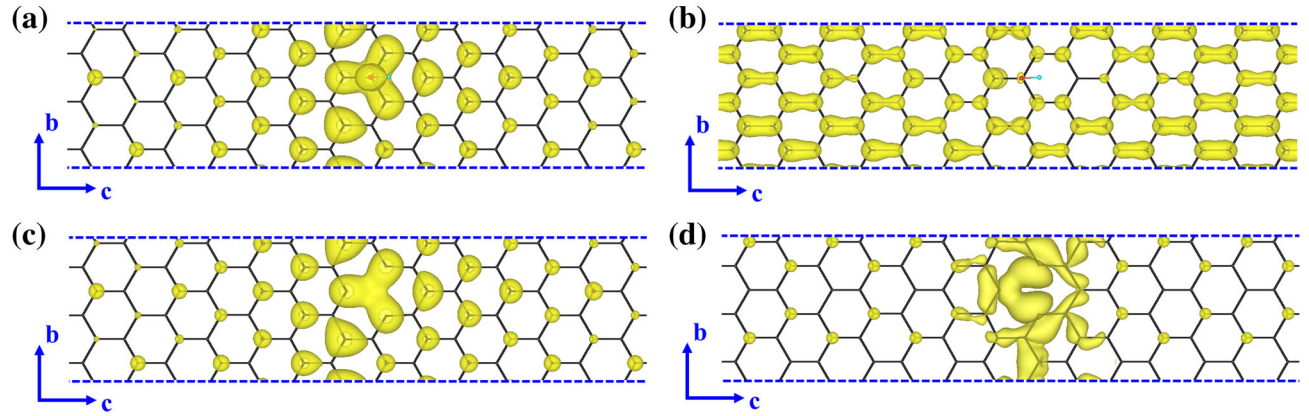

Fig. 5 **a** and **b** are the charge density of HOMO and LUMO of graphene with a hydroxyl. **c** and **d** are the charge density of graphene with a single vacancy. All charge densities are plotted with the same isosurface (1E-3a_0^{-3})

Fig. 6 **a** and **b** are the transmission spectrums at zero bias with different scattering structures shown in Fig. 4b–i, representing low (C/O = 36:1) and high (C/O = 18:1) oxygen concentration, respectively. **c** and **d** are the π-orbital LDOS contours along the transport direction for the model with scattering structures in Fig. 4h, i. The energy origin is set to be the Fermi level

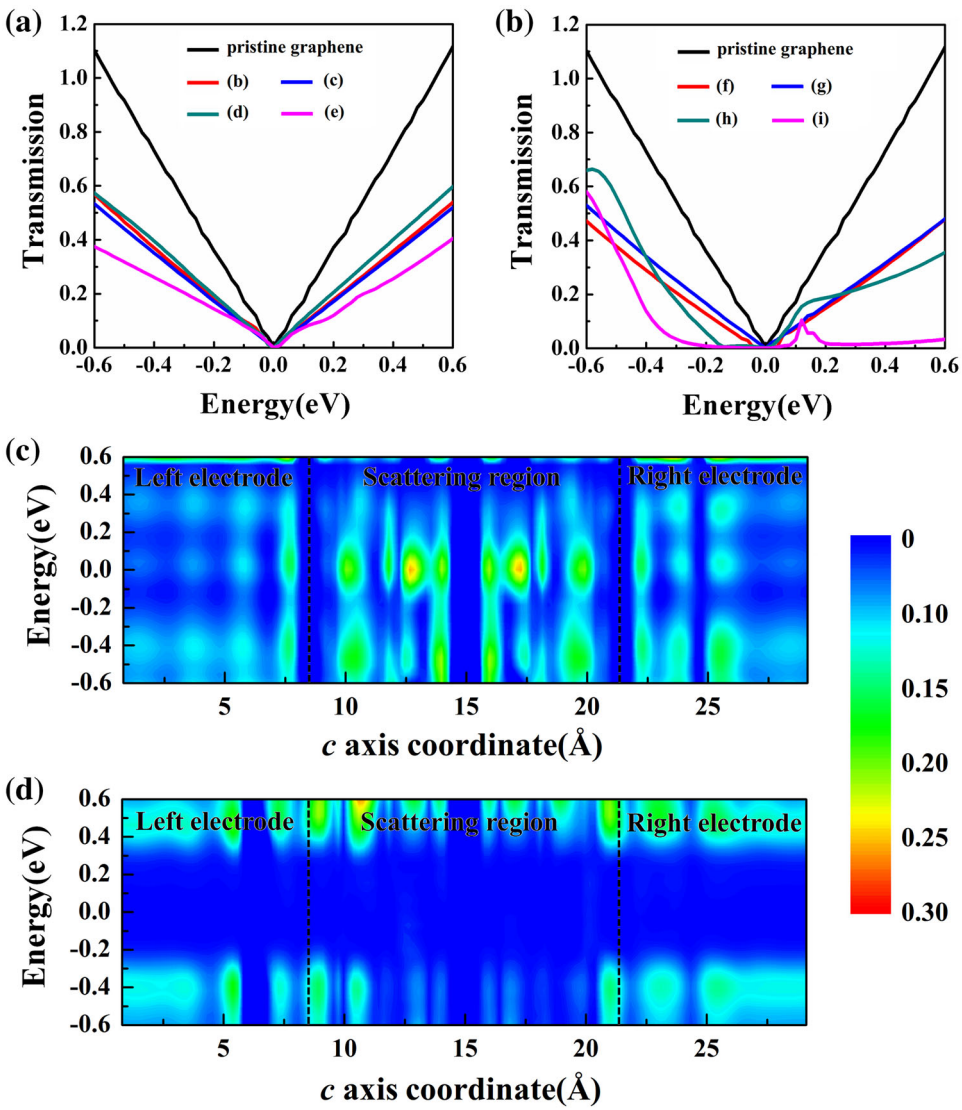

Before the discussion of transport calculations, we have presented the lowest unoccupied molecular orbital (LUMO) and the highest occupied molecular orbital (HOMO) of hydroxyl and those of a SV to discuss their role during the transport process. As shown in Fig. 5, both hydroxyl and SV will cause localization of HOMO. The SV essentially localizes LUMO around it. In contrast, the hydroxyl slightly depletes LUMO in the vicinity, but reserves extension of LUMO to the whole transport region. Our results suggest that the localization of HOMO and/or LUMO will increase scattering to carriers and block transporting channels. Since the SV induces greatly the localization of both HOMO and LUMO, it will cause worse degradation of the electronic transport than hydroxyl group.

The transmission spectrums of structures in Fig. 4b–e are shown in Fig. 6a with C/O of ~36:1. Both pristine graphene and the RGO with low ratios of hydroxyl and/or SV defect remains semimetallic without a transport gap, which is probable because only a single carbon atom is blocked along the electron transport channel. When the hydroxyl is in SV, the conductance shows slight improvement comparing to graphene with SV, which agrees with Lee's results [44]. In contrast, the conductance becomes worse when it is outside of SV. Figure 6b shows transmission spectrum of those with C/O ~18:1, which is close to the real C/O ratio in experiments. The graphene remains semimetallic if there are only two hydroxyl groups in each unit cell, while two isolated SVs without hydroxyl groups open a transport gap about 0.06 eV. However, their transmission coefficients out of the transport gap energy range are similar. These results imply that vacancies may exhibit slightly greater effect on the graphene than the hydroxyl, which is consistent with our discussion about the role of hydroxyl and SV. When both hydroxyl groups and SVs are present, the transport properties are further suppressed. We note that the transport gap increases to about 0.15 eV when two hydroxyl groups locates inside the SVs. It is also observable that when the energy range is out of the transport gap, the transmission coefficients will be comparable to that of graphene with hydroxyl groups or SVs. However, when both hydroxyl groups are out of SVs, the transport gap is more than 0.30 eV. Especially, the transmission coefficients on positive energy will still close to zero. The comparison suggests that the transport is sensitive to the hydroxyl distributions in RGO and is more seriously suppressed if the hydroxyl group is outside of vacancies in the high-concentration case. In order to understand the notable difference of the transport properties of RGO with hydroxyl inside and outside defects, we plot the π-electrons' LDOS along the transport direction (c axis) for the two models with high hydroxyl concentrations, as shown in Fig. 6c, d. The color bar represents the magnitude of DOS of the corresponding c axis coordinate near the Fermi level. It is found that a large amount of π states are localized to the defects near the Fermi level when the hydroxyl groups are inside the SV defects, which result comparable transmission with only hydroxyl groups or SVs in Fig. 6b. In contrast, Fig. 6d shows that no π states appear in the same energy range when these hydroxyl groups stay out of the defects, which means that the transport channels are blocked near the Fermi level and the graphene becomes semiconductivity with a large transport bandgap. As the C/O ratio is close to experimental concentration of RGO, it is assumed that the electronic transport properties should be mostly affected by the hydroxyl away from the defect, which give us a guidance to improve the electronic properties of RGO by removing hydroxyl groups outside the defect rather than inside it.

4 Conclusion

In conclusion, we have systematically studied the effect of SV, DV, and edges on the migration of hydroxyl groups on graphene plane. The spin-polarized charge density along the symmetric path near the defect leads to two types of distinct diffusion energy barriers: one increases monotonously and the other is oscillatory. The presence of defect suppresses the diffusion of the hydroxyl in the vicinity. Moreover, the transport calculations show that the configuration of hydroxyl out of the defect has larger effect on the overall RGO conductance.

Acknowledgments This work is supported National Basic Research Program of China (2013CB934800), National Natural Science Foundation of China (Grant Nos. 51302094 and 51101064), and Fundamental Research Funds for the Central Universities, HUST (2014TS037). Rong Chen acknowledges the Thousand Young Talents Plan and Program for Changjiang Scholars and Innovative Research Team in University. The calculations are done at the Texas Advanced Computing Center (TACC) in the University of Texas in Austin (http://www.tacc.utexas.edu).

References

1. K.S. Novoselov, A.K. Geim, S.V. Morozov, D. Jiang, Y. Zhang, S.V. Dubonos, I.V. Grigorieva, A.A. Firsov, Science **306**, 666 (2004)
2. A.K. Geim, Science **324**, 1530 (2009)
3. S.F. Pei, H.M. Cheng, Carbon **50**, 3210 (2012)
4. H.A. Becerril, J. Mao, Z.F. Liu, R.M. Stoltenberg, Z.N. Bao, Y.S. Chen, ACS Nano **2**, 463 (2008)
5. X.L. Li, H.L. Wang, J.T. Robinson, H. Sanchez, G. Diankov, H.J. Dai, J. Am. Chem. Soc. **131**, 15939 (2009)
6. S.F. Pei, J.P. Zhao, J.H. Du, W.C. Ren, H.M. Cheng, Carbon **48**, 4466 (2010)
7. Y.W. Zhu, W.W. Cai, R.D. Piner, A. Velamakanni, R.S. Ruoff, Appl. Phys. Lett. **95**, 103104 (2009)

8. K. Krishnamoorthy, M. Veerapandian, R. Mohan, S.J. Kim, Appl. Phys. A **106**, 501 (2012)
9. T. Szabó, O. Berkesi, P. Forgó, K. Josepovits, Y. Sanakis, D. Petridis, I. Dékány, Chem. Mater. **18**, 2740 (2006)
10. H.K. Jeong, Y.P. Lee, R.J.W.E. Lahaye, M.H. Park, K.H. An, I.J. Kim, C.W. Yang, C.Y. Park, R.S. Ruoff, Y.H. Lee, J. Am. Chem. Soc. **130**, 1362 (2008)
11. F.C. Liu, T. Tang, Q. Feng, M. Li, Y. Liu, N.J. Tang, W. Zhong, Y.W. Du, J. Appl. Phys. **115**, 164307 (2014)
12. J.I. Paredes, S. Villar-Rodil, P. Solís-Fernández, A. Martínez-Alonso, J.M.D. Tascón, Langmuir **25**, 5957 (2009)
13. S. Park, R.S. Ruoff, Nat. Nanotech. **4**, 217 (2009)
14. C. Gómez-Navarro, R.T. Weitz, A.M. Bittner, M. Scolari, A. Mews, M. Burghard, K. Kern, Nano Lett. **7**, 3499 (2007)
15. S. Stankovich, D.A. Dikin, R.D. Piner, K.A. Kohlhaas, A. Kleinhammes, Y. Jia, Y. Wu, Carbon **45**, 1558 (2007)
16. S. Gilje, S. Han, M. Wang, K.L. Wang, R.B. Kaner, Nano Lett. **7**, 3394 (2007)
17. D.X. Yang, A. Velamakanni, G. Bozoklu, S.J. Park, M. Stoller, R.D. Piner, S. Stankovich, I. Jung, D.A. Field, C.A. Ventrice Jr, R.S. Ruoff, Carbon **47**, 145 (2009)
18. Y.P. Zhang, D.L. Li, X.J. Tan, B. Zhang, X.F. Ruan, H.J. Liu, C.X. Pan, L. Liao, T.Y. Zhai, Y. Bando, S.S. Chen, W.W. Cai, R.S. Ruoff, Carbon **54**, 143 (2013)
19. S. Kim, S. Zhou, Y.K. Hu, M. Acik, Y.J. Chabal, C. Berger, W. de Heer, A. Bongiorno, E. Riedo, Nat. Mater. **11**, 544 (2012)
20. P.V. Kumar, M. Bernardi, J.C. Grossman, ACS Nano **7**, 1638 (2013)
21. C. Gómez-Navarro, J.C. Meyer, R.S. Sundaram, A. Chuvilin, S. Kurasch, M. Burghard, K. Kern, U. Kaiser, Nano Lett. **10**, 1144 (2010)
22. A. Bagri, R. Grantab, N.V. Medhekar, V.B. Shenoy, J. Phys. Chem. C **114**, 12053 (2010)
23. A. Bagri, C. Mattevi, M. Acik, Y.J. Chabal, M. Chhowalla, V.B. Shenoy, Nat. Chem. **2**, 581 (2010)
24. P. Hohenberg, W. Kohn, Phys. Rev. **136**, B864 (1964)
25. W. Kohn, L.J. Sham, Phys. Rev. **140**, A1133 (1965)
26. G. Kresse, J. Hafner, Phys. Rev. B **47**, 558 (1993)
27. G. Kresse, J. Hafner, Phys. Rev. B **49**, 14251 (1994)
28. G. Kresse, J. Hafner, Comput. Mater. Sci. **6**, 15 (1996)
29. J.P. Perdew, K. Burke, M. Ernzerhof, Phys. Rev. Lett. **77**, 3865 (1996)
30. G. Kresse, D. Joubert, Phys. Rev. B **59**, 1758 (1999)
31. H.J. Monkhorst, J.D. Pack, Phys. Rev. B **13**, 5188 (1976)
32. G. Henkelman, H. Jónsson, J. Chem. Phys. **113**, 9978 (2000)
33. J.M. Soler, E. Artacho, J.D. Gale, A. Garcia, J. Junquera, P. Ordejón, D. Sanchez-Portal, J. Phys. Condens. Matter **14**, 2745 (2002)
34. M. Brandbyge, J.L. Mozos, P. Ordejón, J. Taylor, K. Stokbro, Phys. Rev. B **65**, 165401 (2002)
35. A. Svizhenko, M.P. Anantram, T.R. Govindan, B. Biegel, R. Venugopal, J. Appl. Phys. **91**, 2343 (2002)
36. K. Saloriutta, A. Uppstu, A. Harju, M.J. Puska, Phys. Rev. B **86**, 235417 (2012)
37. F. Banhart, J. Kotakoski, A.V. Krasheninnikov, ACS Nano **5**, 26 (2011)
38. A.W. Robertson, G.D. Lee, K. He, E. Yoon, A.I. Kirkland, J.H. Warner, Nano Lett. **14**, 3972 (2014)
39. A.W. Robertson, B. Montanari, K. He, C.S. Allen, Y.A. Wu, N.M. Harrison, A.I. Kirkland, J.H. Warner, ACS Nano **7**, 4495 (2013)
40. N. Ghaderi, M. Peressi, J. Phys. Chem. C **114**, 21625 (2010)
41. S.B. Tang, S.Y. Zhang, Chem. Phys. **392**, 33 (2012)
42. H.J. Xiang, E. Kan, S.H. Wei, M.H. Whangbo, J.L. Yang, Nano Lett. **9**, 4025 (2009)
43. Y.W. Son, M.L. Cohen, S.G. Louie, Phys. Rev. Lett. **97**, 216803 (2006)
44. G. Lee, K.S. Kim, K. Cho, J. Phys. Chem. C **115**, 9719 (2011)
45. Y.F. Dai, S. Ni, Z.Y. Li, J.L. Yang, J. Phys. Condens. Matter **25**, 405301 (2013)
46. H.M. Huang, Z.B. Li, J.C. She, W.L. Wang, J. Appl. Phys. **111**, 054317 (2012)
47. S. Plimpton, J. Comput. Phys. **117**, 1 (1995)
48. A.C.T. van Duin, S. Dasgupta, F. Lorant, W.A. Goddard III, J. Phys. Chem. A **112**, 1040 (2008)